Article

Effect of Germanium Incorporation on the Electrochemical Performance of Electrospun Fe$_2$O$_3$ Nanofibers-Based Anodes in Sodium-Ion Batteries

Beatrix Petrovičová [1], Chiara Ferrara [2,3,*], Gabriele Brugnetti [2], Clemens Ritter [4], Martina Fracchia [5], Paolo Ghigna [5], Simone Pollastri [6], Claudia Triolo [1,3], Lorenzo Spadaro [7], Riccardo Ruffo [2,3] and Saveria Santangelo [1,3,*]

1   Dipartimento di Ingegneria Civile, dell'Energia, dell'Ambiente e dei Materiali (DICEAM), Università Mediterranea di Reggio Calabria, 89122 Reggio Calabria, Italy; beatrix.petrovicova@unirc.it (B.P.); claudia.triolo@unirc.it (C.T.)
2   Dipartimento di Scienza dei Materiali, Università di Milano Bicocca, 20125 Milano, Italy; g.brugnetti@campus.unimib.it (G.B.); riccardo.ruffo@unimib.it (R.R.)
3   National Reference Center for Electrochemical Energy Storage (GISEL), Consorzio Interuniversitario Nazionale per la Scienza e Tecnologia dei Materiali (INSTM), 50121 Firenze, Italy
4   Institut Laue-Langevin, 71 Avenue des Martyrs CS 20156, CEDEX 9, 38042 Grenoble, France; ritter@ill.fr
5   Dipartimento di Chimica, Università degli studi di Pavia, 27100 Pavia, Italy; martina.fracchia02@universitadipavia.it (M.F.); paolo.ghigna@unipv.it (P.G.)
6   Elettra-Sincrotrone Trieste, 34149 Basovizza, Trieste, Italy; simone.pollastri@elettra.eu
7   Istituto di Tecnologie Avanzate per l'Energia (ITAE) del Consiglio Nazionale delle Ricerche (CNR), 98126 Messina, Italy; lorenzo.spadaro@itae.cnr.it
*   Correspondence: chiara.ferrara@unimib.it (C.F.); saveria.santangelo@unirc.it (S.S.)

Featured Application: Authors are encouraged to provide a concise description of the specific application or a potential application of the work. This section is not mandatory.

Abstract: Fe$_2$O$_3$ and Fe$_2$O$_3$:Ge nanofibers (NFs) were prepared via electrospinning and thoroughly characterized via several techniques in order to investigate the effects produced by germanium incorporation in the nanostructure and crystalline phase of the oxide. The results indicate that reference Fe$_2$O$_3$ NFs consist of interconnected hematite grains, whereas in Fe$_2$O$_3$:Ge NFs, constituted by finer and elongated nanostructures developing mainly along their axis, an amorphous component coexists with the dominant α-Fe$_2$O$_3$ and γ-Fe$_2$O$_3$ phases. Ge^{4+} ions, mostly dispersed as dopant impurities, are accommodated in the tetrahedral sites of the maghemite lattice and probably in the defective hematite surface sites. When tested as anode active material for sodium ion batteries, Fe$_2$O$_3$:Ge NFs show good specific capacity (320 mAh g^{-1} at 50 mA g^{-1}) and excellent rate capability (still delivering 140 mAh g^{-1} at 2 A g^{-1}). This behavior derives from the synergistic combination of the nanostructured morphology, the electronic transport properties of the complex material, and the pseudo-capacitive nature of the charge storage mechanism.

Keywords: electrospun fibres; iron (III) oxides; germanium incorporation; sodium-ion batteries; Raman spectroscopy; neutron diffraction; XAS; EXAFS

1. Introduction

Affordable and clean energy represents one of the seventeen sustainable development goals (SDGs) adopted by the 193 members of the United Nations General Assembly five years ago [1]. To ensure the achievement of the SDGs by 2030, countries have introduced their implementation in the own national development programs. These joint actions should allow facing the global energy crisis through a worldwide approach, simultaneously reaching other strictly related SDGs, e.g., the "climate action" (the thirteenth SDG).

Although a recent report has revealed that the "affordable and clean energy" goal (seventh SDG) will not be met by the agreed date [2], there are encouraging signs that energy is becoming more sustainable and available to the global population. Actually, thanks to the impressive advances of renewable energy sources (RESs) in the electricity sector [3], access to electricity in poorer countries is accelerating.

The sustainability of energy production systems represents a challenge in many contexts, including policy and scientific research. The large variety of initiatives undertaken in the latest years to improve efficiency in resource management has greatly boosted the field of energy production from renewable sources, gathering growing attention on electrochemical energy storage (EES) technologies and strongly promoting research in this area [4–14]. The development of cost-effective materials allowing improving power density, cyclability and round-trip efficiency is a key point both for more mature EES devices, such as redox flow batteries [15–18], and for the newer, developing ones, such as post-lithium batteries [18–23]. Presently, research on the latter topic is greatly focused on nanostructured materials [18,24–28]. Among them, electrospun nanomaterials, suitable for production at the large-scale and able to meet requirements of a wide range of EES applications [18,27,28], have been extensively evaluated as active components in post-lithium batteries [18,27–31].

In the scenery of post-lithium rechargeable batteries, the ones exploiting sodium-ion storage, even if not commercialized at the large scale yet, probably represent the technology with the highest level of maturity and sustainability [19,32]. The development of highly performing anode materials is one of the barriers to still be overcome [33]. Transition metal oxides, exhibiting high theoretical reversible capacities and low cost, have broadly been evaluated as anode materials.

Iron (III) oxide that stores sodium ions via the widely agreed $Fe_2O_3 + 6\,Na^+ + 6\,e^- \rightleftarrows 3\,Na_2O + 2\,Fe^0$ conversion mechanism [34,35] has received noticeable attention due to its relevant theoretical specific capacity (1005 and 926 mAhg^{-1} for its α- and γ-phase, respectively [35]), large abundance, environmental friendliness and non-toxicity [35–37]. Nanostructure engineering has been proved to be a viable strategy to cope with detrimental effects of the large volume change experienced during Na^+ intercalation/de-intercalation [35,38]. Incorporating tetravalent impurities in the Fe_2O_3 lattice, a commonly adopted approach to enhance the conductivity of hematite photo-anodes [39–41], has been demonstrated to improve the electrochemical performance of nanostructured Fe_2O_3-based anode materials for sodium-ion batteries (SIBs) [36,37].

This work presents the results of a comprehensive investigation of the effects produced by germanium incorporation in the nanostructure and crystalline phase of electrospun Fe_2O_3 nanofibers (NFs). The electrochemical activity of Fe_2O_3:Ge NFs as active anode material in SIBs is evaluated.

2. Materials and Methods

2.1. Materials

Sigma Aldrich supplied iron (II) acetate, $Fe(C_2H_3O_2)_2$ (purity: 95%; CAS No. 3094-87-9), germanium (IV) isopropoxide, $Ge(OCH(CH_3)_2)_4$ (purity: 97%; CAS No. 21154-48-3), polyacrylonitrile, $(C_3H_3N)_n$ (average molecular weight: 150,000 g mol^{-1}; purity: 99.9%; CAS No. 25014-41-9) and *N,N*-dimethylformamide, $HCON(CH_3)_2$ (anhydrous: 99.8%; CAS No. 68-12-2). As-purchased reagents were utilized for the preparation of the precursor solutions.

2.2. Preparation of the Electrospun NFs

The synthetic route followed to produce the electrospun NFs (Figure S1) was described in detail in previous papers [36,39,42]. Concisely, the spinnable solutions were prepared via sol-gel method. In a typical procedure, 0.325 g polyacrylonitrile (PAN) was dissolved in 4.550 g *N,N*-dimethylformamide (DMF) and a homogeneous solution was obtained after magnetic stirring at room temperature (RT) for 2 h. Then, 0.389 g iron (II) acetate (FeAc$_2$), corresponding to a Fe concentration of 38.5% relative to PAN, was added to prepare the (reference) iron oxide NFs. The Ge-doped iron oxide NFs were prepared by the addition

of 0.350 g FeAc$_2$ and 0.0531 g germanium (IV) isopropoxide (GeIPO), corresponding to a (Fe + Ge) concentration of 38.5% relative to the polymer and to a Ge:Fe mass ratio of 1:9 (corresponding to 0.085 Ge:Fe molar ratio). After 2 h magnetic stirring at RT, the as-prepared solution was loaded into a 20 mL glass syringe equipped with 40 mm long 0.8 gauge stainless-steel needle and electrospun at a DC voltage of 17 kV via a CH-01 Electro-spinner 2.0 (Linari Engineering s.r.l.). Solution was fed at a rate of 23.5 μL min^{-1}. The electrospun NFs were collected on a grounded aluminum foil placed at a distance of 11 cm from the tip of the needle. After drying at RT overnight to remove the DMF residuals, the as-spun fibrous membranes were peeled from the collector and calcined in air for 2 h through a single-step process at 600 °C (heating rate: 5 °C min^{-1}). Upon calcination, the organic components were completely removed from the FeAc$_2$-PAN and GeIPO-FeAc$_2$-PAN NFs and the iron oxide was generated. For further details on the syntheses and experimental setup utilized see refs [36,39,42].

2.3. Characterization

After un-controlled cooling to RT, the as-calcined samples (Figure S2) were analyzed by means of scanning electron microscopy (SEM), transmission electron microscopy (TEM), X-ray diffraction (XRD), powder neutron diffraction (PND), micro-Raman spectroscopy (MRS), X-ray photoelectron spectroscopy (XPS) and X-ray absorption spectroscopy (XAS).

SEM images were acquired on a Zeiss microscope (15 kV), equipped with software for the automated measurement of the NF diameters from their SEM images. A Philips CM 200 microscope (200 kV), equipped with energy-dispersive X-ray (EDX) spectrometer, was utilized for the TEM analysis. XRD patterns were recorded with a Bruker D2 diffractometer using Ni β-filtered Cu-K$_\alpha$ radiation source (λ = 0.1541 nm). Raman scattering was measured in air at RT by means of a NTEGRA—Spectra SPM NT-MDT confocal microscope coupled to a solid-state laser operating at 633 nm. A variable ND filter set the laser power at 250 μW at the sample surface to prevent local heating. The scattered light from the sample, collected by means of a 100X Mitutoyo objective, was detected by a cooled ANDOR iDus CCD Camera. Spectra from several random positions on each specimen were recorded to investigate its spatial homogeneity. The collected spectra were averaged to have a reliable picture of the entire sample. XPS analysis was conducted with a Physical Electronics GMBH PHI 5800-01 spectrometer, equipped with a monochromatic Al-K$_\alpha$ source (1486.6 eV) with a power beam of 300 W. The C 1*s* peak at 284.5 eV was assumed as reference for binding energies. Further details on the instrumentation and experimental data processing can be found elsewhere [36,37,39,42].

The XAS spectra were collected at the Fe and Ge K-edges (7112 and 11,103 eV, respectively) at the XAFS beamline [43] operating at the Elettra synchrotron radiation facility in Trieste, Italy. The spectra were recorded at RT in transmission mode; for the measurements, a proper amount of sample (as to give a unit jump in the absorption coefficient) was mixed with cellulose and pressed into a pellet. Energy calibration was performed measuring the absorption spectrum of either metallic Fe pellet and Ge foil, placed in a second experimental chamber after the sample and after the I1 ionization chamber. The ring current and the energy were 200 mA and 2.4 GeV, respectively. A Si(111) double-crystal monochromator was used, ensuring high-order harmonic rejection by detuning of the second crystal. A water-cooled Pt-coated silicon mirror was used to obtain vertical collimation of the beam. The X-ray signal extraction and analysis, including the linear combination fit, were performed by means of Athena, belonging to the set of interactive programs IFEFFIT [44,45]. For the X-ray absorption near edge structure (XANES) analysis, the raw spectra were first background subtracted using a straight line and normalized to unit absorption above 800 eV, where the extended X-ray absorption fine structure (EXAFS) oscillations are no more visible. The EXAFS data analysis at the Ge K-edge was performed employing the Excurve code using a k2 weighing scheme and isolating the χ(k) signal given by the first shell through Fourier filtering, using a Gaussian window between 0.7 and 2.4 Å.

A PND pattern of the Fe_2O_3:Ge NFs was collected at RT in a vanadium sample holder on the high intensity D20 diffractometer at the Institut Laue-Langevin (ILL), Grenoble, France, with the use of 1.54 Å wavelength, in the 0–150° angular range, using the high-resolution option with a takeoff angle of 90°. Data were analyzed using the FullProf Suite to perform LeBail fitting and traditional Rietveld refinement.

2.4. Electrochemical Measurements

Electrodes based on Fe_2O_3:Ge NFs were obtained by mixing the active material with SuperP carbon black and an organic binder mixture in the weight ratio 6:3:1. The binder consisted of a 1:1 weight mixture of polyacrylic acid and carboxymethylcellulose. The mechanical mixture was dispersed in water and homogenized in an Ultra-turrax batch dispersers. The obtained slurry was then deposited by doctor blade with a wet film thickness of 75 μm on an Al foil. An electrode load of 1.5 mg cm^{-2} was obtained after drying at 140 °C in vacuum for two hours. Round disks of 16 mm in diameter were cut to fabricate 2032 coin cell equipped with a metallic sodium counter electrode and a Whatman glass fiber separator soaked with a solution of 1 M $NaClO_4$ in propylene carbonate. The cell assembling was made in an Ar filled glove box. Potentiodynamic cycling with galvanostatic acceleration (PCGA) and galvanostatic cycling with potential limitation (GCPL) were performed using a Biologic VMP3 potentiostat-galvanostat.

3. Results and Discussion

3.1. Physicochemical Properties of the NFs

Morphological and textural properties of the electrospun NFs were investigated by SEM and TEM analyses (Figure 1). In both types of produced NFs (Fe_2O_3 NFs and Fe_2O_3:Ge NFs), no beads were observed. Nonetheless, the results revealed that the addition of GeIPO to the FeAc$_2$-PAN-DMF precursor solution translated into evident differences in the morphology and texture of the calcined NFs. SEM images showed that the NFs prepared without adding GeIPO had rough and porous surface (Figure 1a,b). Their diameters, as calculated by the image analysis software, varied mainly between 120 and 500 nm, although largely thicker NFs (>0.8 μm) were also present. The center of the diameter distribution was located at 230 nm. Differently, the surface of the germanium-containing NFs was smoother (Figure 1c,d) and their size varied more uniformly in the 65–1180 nm range. The center of the distribution moved at higher values (360 nm). Many factors, such as feeding rate of the solution, applied voltage, collection distance and ambient humidity, affect the morphology and diameters of the fibers. In the present study, feeding rate of the solution, applied voltage and collection distance were kept constant. In addition, the relative air humidity (40%) was the same in the two syntheses. Nonetheless, the well-known extreme moisture sensitivity of the germanium isopropoxide and miscibility of water with DMF might have played a role in giving rise to a more uniform fiber diameter distribution since humidity causes changes in the nanofibers diameter by controlling the solidification process of the charged jet.
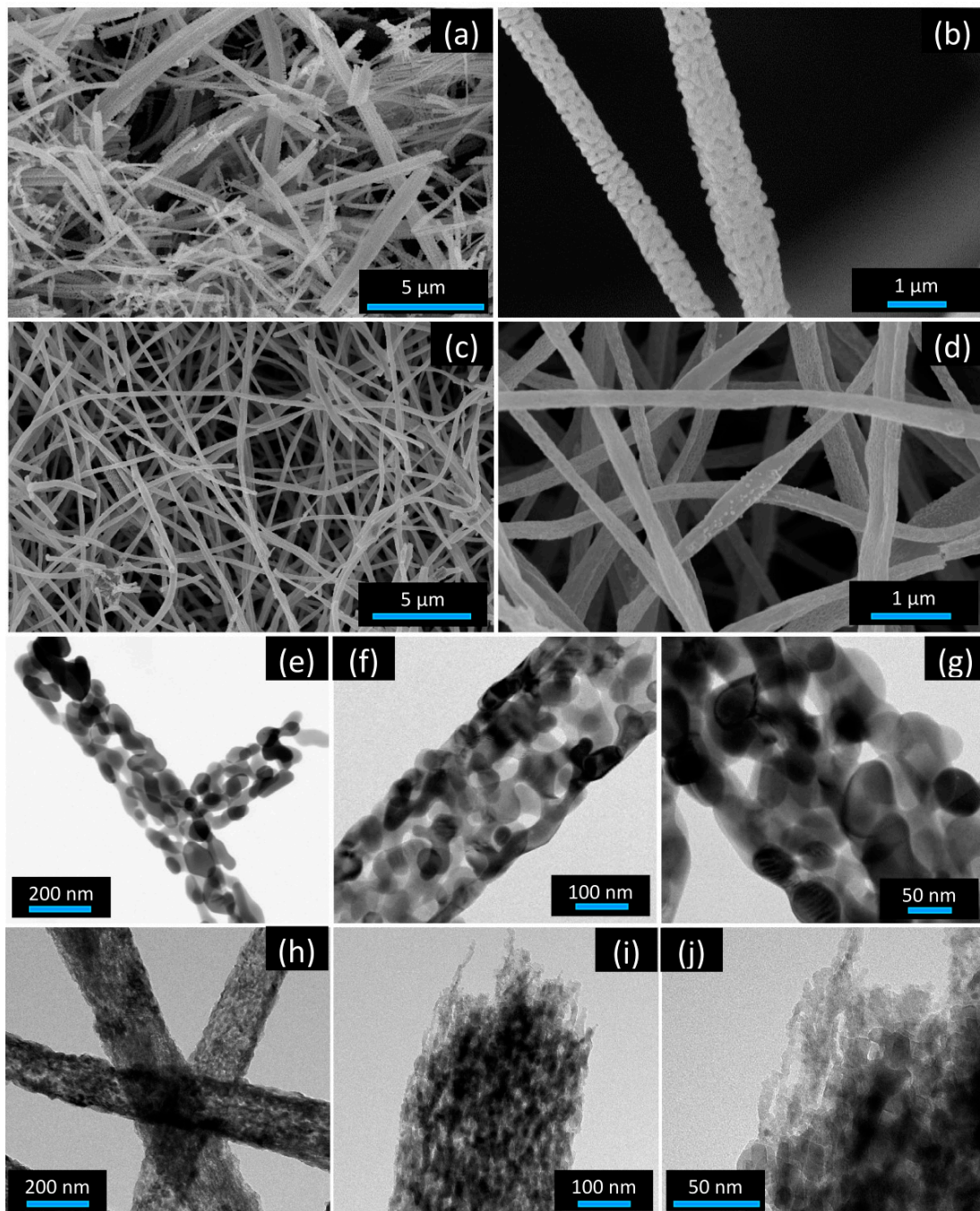
Figure 1. Morphology of the electrospun NFs, as resulting from (**a**–**d**) SEM and (**e**–**j**) TEM analyses. The shown SEM images refer to (**a**,**b**) Fe_2O_3 NFs and (**c**,**d**) Fe_2O_3:Ge NFs. The shown TEM images refer to (**e**–**g**) Fe_2O_3 NFs and (**h**–**j**) Fe_2O_3:Ge NFs.

The TEM analysis shed light on the different texture of the fibers (Figure 1e–j). Although both types of NFs exhibited a hierarchical structure, in the absence of germanium (Figure 1e–g), the NFs consisted of interconnected rounded and smooth crystalline grains, about 65 nm in size [39]. The resulting coral-like architecture seems to be peculiar to electrospun iron oxide NFs, as it has been frequently observed regardless of the precursors utilized to prepare the spinnable solution and the heat treatment conditions [46–53]. Previous studies on NFs prepared under the same conditions [42] had revealed the single-crystal or quasi-single-crystal nature of the oxide grains, as well as the hollow section of the fibers that is due to the large temperature gradient along the radial direction experienced by the $FeAc_2$-PAN NFs upon calcination [54]. Different from the pure iron oxide NFs, the

germanium-containing ones consisted of finer and elongated nanostructures that developed mainly along the longitudinal axis of the fiber (Figure 1h–j). A hierarchical structure with similar characteristics had been previously reported for electrospun Si-doped iron oxide NFs [36]. Indeed, both silicon and germanium are believed to drive the growth along preferential crystallographic directions to a limited extent [41,55,56].

The spatial distribution of the NF components was investigated via TEM/EDX (Figure S3). The elemental maps revealed a homogeneous distribution of iron, oxygen and germanium within the NFs, with no organic residuals from the pristine NFs.

The oxide phase in the NFs and its crystallinity were investigated by X-ray and neutron diffraction and MRS analyses. Figure S4 compares the diffraction patterns of the NFs produced from the $FeAc_2$-PAN-DMF and GeIPO-$FeAc_2$-PAN-DMF solutions. In the former case, all detected peaks were ascribable to the reflections from crystallographic planes of rhombohedral hematite (α-Fe_2O_3, JCPDS card no. 33-0664.), indicating the formation of a single crystalline phase, as expected on the basis of previous studies [36,39,42] and literature [46,47,49,51–53,57] as well. The average crystallite size (30.4 nm) was estimated from the FWHM (full width at half-maximum, β) of the most intense (104) peak, via the Scherrer formula, $d = K\lambda\beta\cos\theta$, with K = 0.9 and λ = 0.1541 nm. In the X-ray diffractogram of the germanium-containing NFs, the peaks indexed to α-Fe_2O_3 were weaker and broader. In addition, the diffraction peaks typical of γ-phase of the iron (III) oxide (maghemite, JCPDS No.39-1346) were detected [58–60]. The estimation of the average crystallite size from the (104) peak FWHM gave a smaller value (18.1 nm) with respect to the pure oxide, in good agreement with the TEM analysis and literature reports on doped Fe_2O_3 [61–63] as well. Finally, the detection of a very broad background in the pattern of Ge-containing NFs suggested the presence of an amorphous component.

Figure 2 compares the micro-Raman spectra of Fe_2O_3 and Fe_2O_3:Ge NFs, as resulting from the average on different random locations in each specimen. The group theory predicts seven normal phonon modes for α-Fe_2O_3 [64–66], namely two "external" modes involving the translations and rotations of entire Fe_2O_3 units ($E_g(1)$ and $E_g(2)$ at 245 and 294 cm^{-1}, respectively) and five "internal" modes associated to the motion within a single $Fe(O)_6$ octahedral unit ($A_{1g}(1)$, $E_g(3)$, $E_g(4)$, $A_{1g}(2)$ and $E_g(5)$ at 225, 298, 412, 500, and 612 cm^{-1}, respectively) [67–69]. In addition, the peaks originating from these modes, a strong asymmetrical band peaking at ~1320 cm^{-1} and two weak features at ~660 and ~830 cm^{-1} were detected in the spectrum of the Fe_2O_3 NFs. The peak at ~660 cm^{-1} is associated to the IR-active longitudinal optical (LO) E_u mode, activated by disorder (grain size, defects, heteroatoms) in the hematite lattice [36,42,55,64,66,69,70], while the asymmetrical band has been recently ascribed to its overtone [66,67,69]. The peak at ~830 cm^{-1} is assigned to the photo-excitation of a spin-wave (one-magnon mode, 1M) in the canted antiferromagnetic structure of α-Fe_2O_3 [66,71]. Spectra collected from different random locations in the reference sample (not shown) did not significantly differ from each other, evidencing the spatially uniform formation of hematite.

Five Raman-allowed phonon modes ($A_{1g} + E_g + 3T_{2g}$) are predicted for the γ-polymorph of iron (III) oxide having a spinel crystalline structure [65,72], similarly to magnetite (Fe_3O_4). Nonetheless, in maghemite, a Fe-deficient form of Fe_3O_4 (Fe^{3+}_{th} [$Fe_{5/3}^{3+} \square_{1/3}]_{oh}O_4^{-2}$, with $\square$ denoting a Fe-vacancy and *th* and *oh* indicating tetrahedral and octahedral sites, respectively), the peaks are broader [72]. Indeed, three peaks are usually detected (T_{1g}, E_g and A_{1g} at ~360, ~510 and ~705 cm^{-1}, respectively) in γ-Fe_2O_3, along with the band originating from 1M photo-excitation at ~1430 cm^{-1} [73,74]. In the spectrum of Fe_2O_3:Ge NFs (Figure 2), the peaks of both α- and γ-phase of the iron oxide were clearly visible, in full agreement with the evidences of XRD analysis. On the contrary, no obvious peak ascribable to germanium dioxide was detected. Spectra recorded at different random locations were different from each other (Figure S5), indicating that the incorporation of germanium led to the spatially non-uniform formation of α- and γ-polymorphs of the oxide.
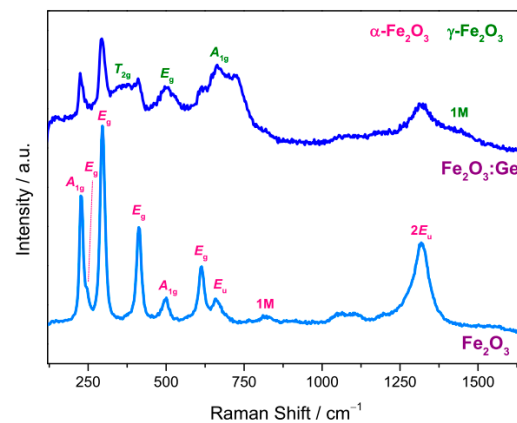
Figure 2. Micro-Raman spectra of the electrospun NFs, as resulting from the average on different random locations in each specimen.

Figure 3a displays the X-ray photoelectron spectra of Fe $2p$ core level in the electrospun NFs. The spectrum of Fe_2O_3 NFs consisted of two spin-orbit components at binding energies of 710.5 eV ($2p_{3/2}$) and 724.0 eV ($2p_{1/2}$) and of two Fe^{3+} shake-up satellites at 718.3 and 732.1 eV, as typical of hematite [63,75]. In agreement with the literature [36,41,56], the incorporation of germanium in the iron oxide lattice did not caused appreciable variations in the spectral profile, but a slight shift (~0.4 eV) of spin-orbit doublets and shake-up satellites towards higher binding energies, for which both co-formation of maghemite [76] and incorporation of germanium [41] could have been responsible. In the Fe_2O_3:Ge NFs, the binding energy position of the Ge $2p_{3/2}$ (1220 eV, inset to Figure 3a) and Ge $3d$ (32 eV, not shown) core levels evidenced the presence of Ge ions with +4 oxidation state [77–79].
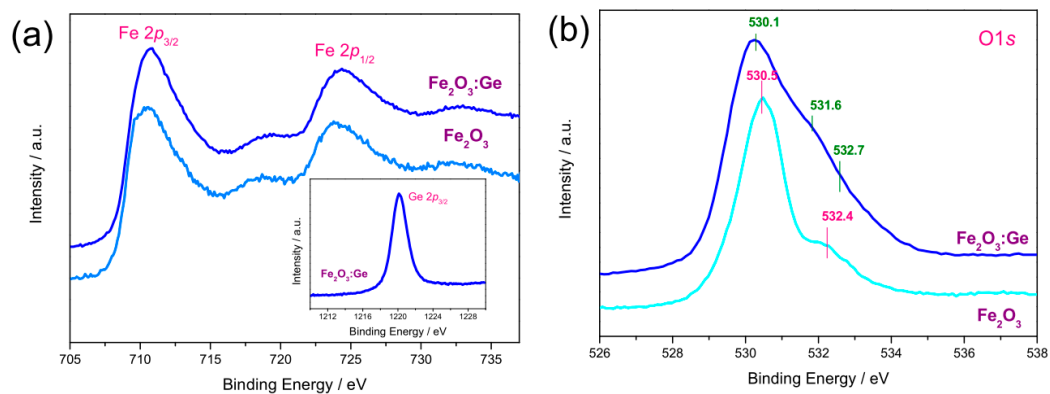
Figure 3. X-ray photoelectron spectra of (**a**) Fe 2p and (**b**) O 1s core levels. Inset to plot (**a**): Ge 2p core level in Fe_2O_3:Ge NFs.

O 1s core level of the two samples exhibited evident differences both in terms of binding energy and shape (Figure 3b), hinting at different surrounding cations. Two components at 530.5 (O_I) and 532.7 eV (O_{II}) were singled out in the spectrum of Fe_2O_3 NFs (Figure S6a); they were ascribed to O_2^- ions of the surface lattice oxygen in α-Fe_2O_3 matrix and to surface hydroxyl (Fe–OH) groups, respectively [80]. The spectrum of Fe_2O_3:Ge NFs exhibited larger broadening (Figure 3b), mirroring the presence of more kinds of oxygen species [81] and clearly pointing out the incorporation of Ge ions into the γ-Fe_2O_3 lattice (i.e., solid solutions), as well as the co-presence of segregate phases of γ-Fe_2O_3 and GeO_2 oxides [81,82]. In maghemite, surface lattice oxygen has been reported to contribute to the O1s intensity at lower binding energy compared with hematite [83,84], whereas the O1s peak of germanium dioxide has been detected at 531.8 eV [77]. Thus, in agreement with the results of XRD and MRS analyses, not only Fe–O species in α-Fe_2O_3 nanocrystals, but also surface lattice oxygen in γ-Fe_2O_3 and GeO_2 phases were identified in the O1s spectrum of Fe_2O_3:Ge NFs, as well as surface hydroxyl groups (Figure S6b). The different

oxygen species were quantified assuming that the contributions at lower bindings energies (530.1–531.6 eV), O_{Ia} and O_{Ib}, originate from Fe–O and Ge–O lattice oxygen, respectively, whereas the signal at higher binding energy (532.7 eV), O_{II}, is related to either the presence of molecular oxygen weakly bounded or oxygen from adsorbed species (e.g., hydroxyl species) [81]. Accordingly, the concentrations of the three species were estimated to be 57.6% (O_{Ia}), 31.4% (O_{Ib}) and 11.0% (O_{II}). Therefore, considering that the fraction of oxygen relating to the isolated GeO_2 phase (OI_b) is 31.4%, being the atomic surface abundance of oxygen 68.8%, that of germanium 10.9% (Table S1) and the stoichiometric ratio between oxygen and germanium of 2:1, it followed that almost all of the Ge ions on the surface of the Fe_2O_3:Ge NFs should be involved in the formation of the oxide phase (Table S2).

Thus, summarizing, the XRD, XPS, and MRS analyses indicated that Fe_2O_3 NFs can be considered as a single-phase compound; differently, the Fe_2O_3:Ge NFs are more complex, both in terms of phase composition and compositional homogeneity, being composed by at least two crystalline phases, and an amorphous component.

To further explore the compositional and structural aspects of Fe_2O_3:Ge NFs, X-ray absorption spectroscopy and neutron diffraction analysis were carried out.

XAS measurements were acquired on Fe_2O_3:Ge NFs at the Fe and Ge K-edges, aiming at selectively obtaining electronic and structural information on both atomic species. The XANES region gives direct indication of the oxidation state; moreover, its fingerprinting properties allow discerning between different species by rapid comparison with the spectra of reference materials. For this purpose, Figure 4a compares the XANES spectrum of the sample at the Fe K-edge with those of hematite (α-Fe_2O_3) and maghemite (γ-Fe_2O_3) [85]. The energy position of the rising edge is indicative of the oxidation state of the sample: in this case, the edge energy of Fe_2O_3:Ge NFs, marked as a black dotted line, was the same as in α- and γ-Fe_2O_3, indicating that all iron is present as Fe(III), in agreement with results of XPS analysis. All the spectral features in the spectrum were attributable either to maghemite or hematite; for a quantification of the effective composition, a linear combination fit was performed (see Figure S7). The best fit, obtained with 77 (1)% maghemite and 23 (1)% hematite, showed a very good agreement with the experimental signal. However, the presence of a small amount of iron-based oxyhydroxide species, especially γ-FeOOH (lepidocrocite) and ferrihydrite, which present some spectral features in the same energy region as maghemite [86,87], could not be excluded.
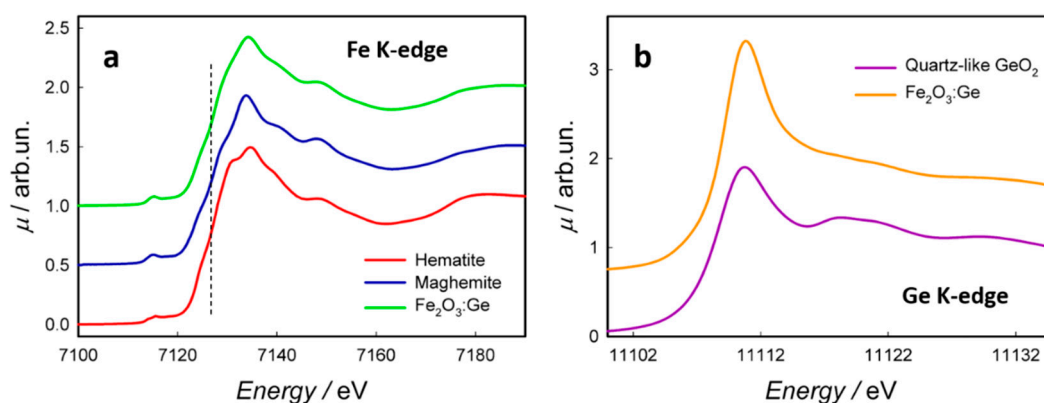
Figure 4. (**a**) XANES spectra at the Fe K-edge of Fe_2O_3:Ge NFs, hematite and maghemite (these last spectra taken from ref [85]. The spectra are shifted along the *y*-axis for better comparison. The absorption edge energy, common to all the three spectra, is indicated as a black dotted line. (**b**) XANES spectra at the Ge K-edge of Fe_2O_3:Ge NFs and of quartz-like GeO_2. The spectra are shifted along the *y*-axis for better comparison.

Figure 4b compares the spectrum of Fe_2O_3:Ge NFs at the Ge K-edge with the reference spectrum of GeO_2 in the quartz-like structure. The edge energy position was coincident in the two spectra, indicating that Ge has oxidation state 4+, in full agreement with the XPS analysis. All the spectral features were visibly broadened in Fe_2O_3:Ge NFs, as expected

for nanosized and/or amorphous samples, and displayed a striking similarity. At the Ge K-edge, the main absorption peak (white line, WL) at 11,112 eV is due to the transition from filled 1s orbitals to empty 4p orbitals. The WL of the spectrum of Fe_2O_3:Ge NFs, as well as for quartz-like GeO_2, was unique and intense, as expected in case of tetrahedral coordination. Indeed, when Ge is in an octahedral environment (e.g., in rutile-like GeO_2), the WL is broadened and split into three distinct features [88,89].

In order to gain further evidence on the coordination around Ge, the EXAFS signal and the corresponding Fourier transform (FT) were extracted (Figure S8a,b). The FT showed an intense peak around 1.7 Å, due to the first Ge-O distance, while all the other contributions above 3 Å became negligible, confirming the amorphousness of the Ge local environment. The $x(k)$ signal resulting from the first shell was isolated through a Fourier-filtering process and fitted, allowing to selectively consider the contribution of the first neighboring atoms around the photoabsorber. The Fourier filtered signal and the fit are shown in Figure S8c,d. The best fit was obtained starting from a GeO_4 structural model; the Ge-O distance was found to be 1.771 (6) Å, in good agreement with the crystallographic distance in quartz-like GeO_2. The parameters of the EXAFS fit are reported in Table S3. In summary, all the XAS evidences pointed towards the presence of Ge(IV) in fourfold coordination, strongly suggesting that Ge is hosted in the tetrahedral sites of the maghemite spinel structure.

PND data were analyzed on the base of the phases identified by XRD, XAS and MRS; hence, to properly fit the pattern, the hematite and maghemite structures were introduced. The final Rietveld refinement is presented in Figure 5. With respect to the XRD pattern, the neutron data showed strong extra reflections (e.g., 17°–26° range, 51° in Figure 5) associated to the magnetic structure of hematite [90]; this magnetic structure was introduced and considered in the refinement as an independent magnetic phase [91].
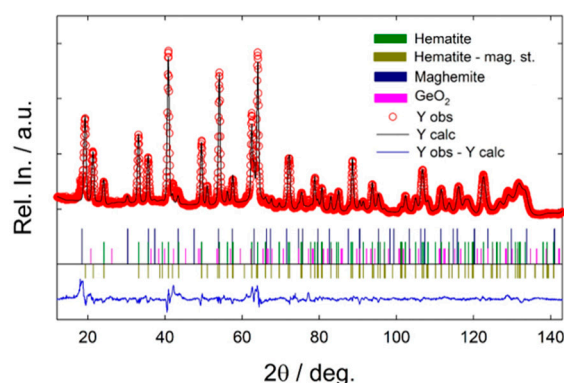
Figure 5. Rietveld refinement of the PND pattern of Fe_2O_3:Ge NFs (χ^2 = 22.0, R_p = 1.97, R_{wp} = 2.39). Hematite 91.1%, Maghemite 8.6%, GeO_2 0.3%. Structural parameters: Hematite a = 5.031 (1) Å, c = 13.7416 (4) Å; Maghemite a = 8.33041 (41) Å.

As the maghemite phase, cubic (S.G. Fd3m and P4$_3$32) and tetragonal (S.G. P4$_1$2$_1$2) polymorphs had been reported in order to account for the ordering of the Fe vacancies [92]. A preliminary Le Bail fit, considering the different maghemite polymorphs, led to identification of the Fd3m phase as the one able to properly account for most of the observed reflections. On this base, Rietveld refinements were performed using the hexagonal α-Fe_2O_3 and the cubic γ-Fe_2O_3 structures. The attempts to refine the scale of GeO_2 as a possible impurity led to very small amount of the oxide, in good agreement with the results of MRS analysis. This finding indicated that most of germanium was successfully dispersed in the iron oxide phase(s) as a dopant.

Results obtained from XAS clearly indicated the presence of Ge in tetrahedral coordination. Based on these indications, for the refinement of neutron data, germanium was considered only in the maghemite structure (the only one where FeO_4 sites are present). However, this scenario was not compatible with the nominal Fe:Ge molar ratio (11.7:1), as all performed refinements led to >85% α-Fe_2O_3 and <15% γ-Fe_2O_3, which should imply

a quantitative Ge substitution in the maghemite structure. Nevertheless, the maghemite phase is characterized by a magnetic structure at RT, but the quality of the experimental data did not allow for the determination of such structure and for its subsequent refinement. Due to the complexity of the system, the results obtained from the neutron diffraction gave only a partial vision of the actual phases and composition. It was concluded that the Fe_2O_3:Ge NFs were composed by α-Fe_2O_3 and γ-Fe_2O_3, as dominant phases, and of an amorphous component with similar chemical composition. Most of germanium was accommodated in the tetrahedral sites of the maghemite structure, even if also the hematite phase could accept Ge dopant, probably on the defective surface sites as no GeO_6 species (that should be associated to the bulk α-Fe_2O_3) were revealed. These results were consistent with previous report on the possibility to obtain α- and γ-phases of iron oxides, respectively oxidized and fully oxidized, upon calcination in air above 500 °C of a hydrated precursor [93]. Results reported in the present work suggested that the incorporation of germanium could drive the phases' formation, with the stabilization of the γ-polymorph, generally not expected at 600 °C.

3.2. Electrochemical Properties of the NFs

PCGA measurements were performed to get cathodic and anodic profiles in quasi-reversible conditions. In this technique, the potential (ranging from 3.0 to 0.01 V vs. Na^+/Na) is decreased (cathodic branch) or increased (anodic branch) by 4 mV and, for each step, the charge is collected until the current becomes less than 20 mA g^{-1}. Considering the theoretical specific capacity of hematite (1005 mAh g^{-1}), the current threshold corresponds to C/50, which should allow to collect all the available charge. The corresponding profiles are reported in Figure 6a. The first cycle Coulomb efficiency was 55%, probably due to both the large amount of carbon at the electrode and the conversion reactions already discussed for similar phases [36]. After the first cycle, the profiles showed the typical pseudocapacitive behavior of these composites, with three different regions of different slopes. After the initial cycle, the specific capacities were around 300 mAh g^{-1}.
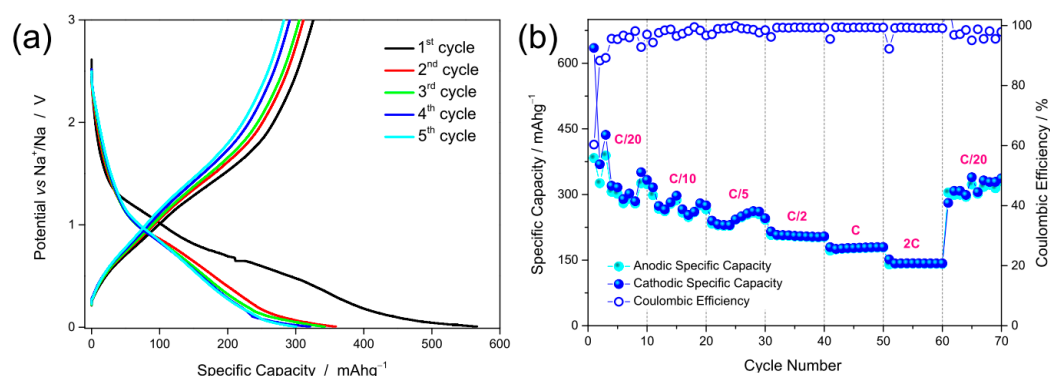
Figure 6. Electrochemical properties of the Fe_2O_3:Ge NFs. (**a**) Potential profiles versus the specific capacity and (**b**) anodic and cathodic specific capacities versus number of cycles at different rates and corresponding Coulombic efficiency.

Galvanostatic cycling was performed to evaluate the rate capability and the capacity retention of the electrodes (Figure 6b). The GCPLs at low currents (C/20) confirmed the capacities observed in PCGA, with an average value of 320 mAh g^{-1} in the anodic process. The large uncertainty of the low current capacities (C/20 and C/10) can be attributed to the intrinsic multi-phase nature of the doped oxide, because the different phases have probably different kinetics affecting the extension of reaction with the sodium ions cycle by cycle. At higher rates, the data precision increases, because the slower phases became less active and do not substantially contribute to the value. The capacity decreased with the C rate, and 270, 240, 205, 175, and 140 mAh g^{-1} were obtained at C/10, C/5, 1C, and 2C, respectively. On the contrary, the Coulomb efficiencies increased with the current (from 94% at C/20 to 99.2% at 2C), pointing out the presence of parasitic cathodic processes

with lower kinetic compared to the charge accumulation reaction. After the 60th cycle (2C), the current was set back to C/20 to evaluate the capacity retention after 70 cycles, which was calculated as 97% with a good and stable recovering of the initial value. Thus, the electrodes showed good specific capacity as anode for sodium ion batteries, with excellent rate capability (140 mAh g^{-1} at 2C which corresponds to 2 A g^{-1}) thanks to the synergistic combination of the electronic transport properties of the complex material, the nanostructured morphologies and the pseudo-capacitive nature of the charge storage mechanism. These performances exceeded those of pure hematite and were in agreement with those obtained from metalloid-doped hematites [36] (Figure S9). Since Fe_2O_3:Ge NFs and Fe_2O_3:Si NFs were prepared by using the same dopant:iron mass ratio (1:9), the larger relative amount of silicon incorporated in the Fe_2O_3 lattice may partly account for the higher specific capacity of Fe_2O_3:Si NFs at lower rates. In any case, the different percentages of α-Fe_2O_3 and γ-Fe_2O_3 (and amorphous) phases present in the Fe_2O_3:Si NFs and Fe_2O_3:Ge NFs made it hard to make a direct comparison considering only the atomic chemical physical properties.

To test the cyclability of the materials at constant current, 180 cycles at C/10 (70 mA g^{-1}) have been performed (Figure S10). The initial capacity values are in agreement with the rate test of Figure 6b, with an average value of 230 $\pm$ 10 mAh g^{-1} (cycles 1–5). Upon cycling, the material shows a constant decrease of the performances of 0.75 mAh g^{-1} per cycle, with capacity retentions of 54% and 42% after 100 and 180 cycles, respectively. These unsatisfactory results are mainly due, as already discussed in Ref. [36], to the binder instability, which tends to crystallize upon cycling.

4. Conclusions

The thorough characterization of the investigated electrospun Fe_2O_3 and Fe_2O_3:Ge NFs via SEM, TEM, MRS, XPS, X-ray and neutron diffraction and XAS allow concluding that:

- Reference Fe_2O_3 NFs, exhibiting grainy structure, consist exclusively of hematite.
- Fe_2O_3:Ge NFs have a more complex architecture and composition. They are formed by finer and elongated nanostructures developing mainly along the fiber axis; although α-Fe_2O_3 and γ-Fe_2O_3 are the dominant phases, an amorphous component is also present.
- Germanium, mostly dispersed as an ionized impurity (with 4+ oxidation state), occupies the tetrahedral sites of the maghemite lattice and probably the defective hematite surface sites.
- The synergy between nanostructured morphology and electronic transport properties of Fe_2O_3:Ge NFs, together with the pseudo-capacitive nature of the charge storage mechanism, are responsible for their excellent rate capability as anode for SIBs (140 mAh g^{-1} at 2C).

Supplementary Materials: The following are available online at https://www.mdpi.com/2076-3417/11/4/1483/s1, Figure S1: Sketch of the synthesis route followed to produce the electrospun iron oxide NFs, Figure S2: Photo of the as-calcined Fe_2O_3 and Fe_2O_3:Ge NFs., Figure S3: Elemental composition of the NFs, Figure S4: XRD patterns of the investigated NFs, Figure S5: Micro-Raman spectra, as measured at different random locations in the sample, Figure S6: Deconvolution of the O 1*s* core level profiles of Fe_2O_3 NFs and Fe_2O_3:Ge NFs, Figure S7: Linear combination fit of the spectrum of Fe_2O_3:Ge NFs acquired at the Fe K-edge, Figure S8: EXAFS signal and Fourier transform for the spectrum of Fe_2O_3:Ge NFs at the Ge K-edge, Figure S9: Results of the rate capability test on Fe_2O_3:Ge NFs, compared with previously investigated Fe_2O_3 and Fe_2O_3:Si NFs, Figure S10. Results of the cyclability test on Fe_2O_3:Ge NFs. Table S1: Surface composition of the NFs, Table S2: Binding energies and fractional area of the components of O 1*s* core level in the NFs, Table S3: parameters of the EXAFS fit.

References

1. UN. Historic New Sustainable Development Agenda Unanimously Adopted by 193 UN Members. 2015. Available online: https://www.un.org/sustainabledevelopment/blog/2015/09/historic-new-sustainable-development-agenda-unanimously-adopted-by-193-un-members (accessed on 9 December 2020).
2. World Bank. *Tracking SDG7: The Energy Progress Report 2018*; The World Bank: Washington, DC, USA, 2018. Available online: https://openknowledge.worldbank.org/handle/10986/29812 (accessed on 9 December 2020).
3. Zekry, A.; Shaker, A.; Salem, M. *Advances in Renewable Energies and Power Technologies: Solar and Wind Energies*; Yahyaoui, I., Ed.; Elsevier Science: Amsterdam, The Netherlands, 2018; Volume 1.
4. Sui, Y.; Zhou, J.; Wang, X.; Wu, L.; Zhong, S.; Li, Y. Recent advances in black-phosphorus-based materials for electrochemical energy storage. *Mater. Today* **2020**. [CrossRef]
5. Zeng, X.X.; Xu, Y.T.; Yin, Y.X.; Wu, X.W.; Yue, J.; Guo, Y.G. Recent advances in nanostructured electrode-electrolyte design for safe and next-generation electrochemical energy storage. *Mater. Today Nano* **2019**, *8*, 100057. [CrossRef]
6. Hou, R.; Liu, B.; Sun, Y.; Liu, L.; Meng, J.; Levi, M.D.; Yan, X. Recent advances in dual-carbon based electrochemical energy storage devices. *Nano Energy* **2020**, *72*, 104728. [CrossRef]
7. Jin, W.; Maduraiveeran, G. Recent advances of porous transition metal-based nanomaterials for electrochemical energy conversion and storage applications. *Mater. Today Energy* **2019**, *13*, 64–84. [CrossRef]
8. Srinivasan, S.S.; Stefanakos, E.K. Clean Energy and Fuel Storage. *Appl. Sci.* **2019**, *9*, 3270. [CrossRef]
9. Bhalothia, D.; Krishnia, L.; Yang, S.S.; Yan, C.; Hsiung, W.H.; Wang, K.W.; Chen, T.Y. Recent advancements and future prospects of noble metal-based heterogeneous nanocatalysts for oxygen reduction and hydrogen evolution reactions. *Appl. Sci.* **2020**, *10*, 7708. [CrossRef]
10. Li, Y.; Zhang, Z.; Duan, D.; Han, Y.; Wang, K.; Hao, X.; Wang, J.; Liu, S.; Wu, F. An Integrated Structural Air electrode based on parallel porous nitrogen-doped carbon nanotube arrays for rechargeable Li–air batteries. *Nanomaterials* **2019**, *9*, 1412. [CrossRef]
11. Fedoseeva, Y.V.; Lobiak, E.V.; Shlyakhova, E.V.; Kovalenko, K.A.; Kuznetsova, V.R.; Vorfolomeeva, A.A.; Grebenkina, M.A.; Nishchakova, A.D.; Makarova, A.A.; Bulusheva, L.G.; et al. Hydrothermal activation of porous nitrogen-doped carbon materials for electrochemical capacitors and sodium-ion batteries. *Nanomaterials* **2020**, *10*, 2163. [CrossRef]
12. Amrouche, S.O.; Rekioua, D.; Rekioua, T.; Bacha, S. Overview of energy storage in renewable energy systems. *Int. J. Hydrogen Energy* **2016**, *41*, 20914–20927. [CrossRef]
13. Pan, F.; Wang, Q. Redox species of redox flow batteries: A review. *Molecules* **2015**, *20*, 20499–20517. [CrossRef]
14. Alotto, P.; Guarnieri, M.; Moro, F. Redox flow batteries for the storage of renewable energy: A review. *Renew. Sust. Energ. Rev.* **2014**, *29*, 325–335. [CrossRef]
15. Busacca, C.; Di Blasi, O.; Briguglio, N.; Ferraro, M.; Antonucci, V.; Di Blasi, A. Electrochemical performance investigation of electrospun urchin-like V_2O_3-CNF composite nanostructure for vanadium redox flow battery. *Electrochim. Acta* **2017**, *230*, 174–180. [CrossRef]
16. Di Blasi, A.; Busacca, C.; Di Blasi, O.; Briguglio, N.; Antonucci, V. Synthesis and characterization of electrospun nickel-carbon nanofibers as electrodes for vanadium redox flow battery. *J. Electrochem. Soc.* **2018**, *165*, A1478. [CrossRef]
17. Busacca, C.; Di Blasi, O.; Giacoppo, G.; Briguglio, N.; Antonucci, V.; Di Blasi, A. High performance electrospun nickel manganite on carbon nanofibers electrode for vanadium redox flow battery. *Electrochim. Acta* **2020**, *355*, 136755. [CrossRef]
18. Santangelo, S. Electrospun nanomaterials for energy applications: Recent advances. *Appl. Sci.* **2019**, *9*, 1049. [CrossRef]

19. Sawicki, M.; Shaw, L.L. Advances and challenges of sodium ion batteries as post lithium ion batteries. *RSC Adv.* **2015**, *5*, 53129–53154. [CrossRef]

20. Wang, F.; Wu, X.; Li, C.; Zhu, Y.; Fu, L.; Wu, Y.; Liu, X. Nanostructured positive electrode materials for post-lithium ion batteries. *Energy Environ. Sci.* **2016**, *9*, 3570–3611. [CrossRef]

21. Choi, J.W.; Aurbach, D. Promise and reality of post-lithium-ion batteries with high energy densities. *Nat. Rev. Mater.* **2016**, *1*, 16013. [CrossRef]

22. Kulova, T.L.; Fateev, V.N.; Seregina, E.A.; Grigoriev, A.S. A Brief review of post-lithium-ion batteries. *Int. J. Electrochem. Sci* **2020**, *15*, 7242–7259. [CrossRef]

23. Wang, B.; Ang, E.H.; Yang, Y.; Zhang, Y.; Ye, M.; Liu, Q.; Li, C.C. Post-lithium ion battery era: Recent advances in rechargeable potassium-ion batteries. *Chem. Eur.* **2021**, *27*, 512–536. [CrossRef]

24. Liang, Y.; Lai, W.H.; Miao, Z.; Chou, S.L. Nanocomposite materials for the sodium–ion battery: A review. *Small* **2018**, *14*, 1702514. [CrossRef]

25. Li, F.; Zhou, Z. Micro/nanostructured materials for sodium ion batteries and capacitors. *Small* **2018**, *14*, 1702961. [CrossRef]

26. Fang, Y.; Yu, X.Y.; Lou, X.W.D. Nanostructured electrode materials for advanced sodium-ion batteries. *Matter* **2019**, *1*, 90–114. [CrossRef]

27. Wang, L.; Yang, G.; Peng, S.; Wang, J.; Yan, W.; Ramakrishna, S. One-dimensional nanomaterials toward electrochemical sodium-ion storage applications via electrospinning. *Energy Storage Mater.* **2020**, *25*, 443–476. [CrossRef]

28. Wang, Y.; Liu, Y.; Liu, Y.; Shen, Q.; Chen, C.; Qiu, F.; Li, P.; Jiao, L.; Qu, X. Recent advances in electrospun electrode materials for sodium-ion batteries. *J. Energy Chem.* **2021**, *54*, 225–241. [CrossRef]

29. Janakiraman, S.; Khalifa, M.; Biswal, R.; Ghosh, S.; Anandhan, S.; Venimadhav, A. High performance electrospun nanofiber coated polypropylene membrane as a separator for sodium ion batteries. *J. Power Sources* **2020**, *460*, 228060. [CrossRef]

30. Tian, S.; Jiang, Q.; Cai, T.; Wang, Y.; Wang, D.; Kong, D.; Ren, H.; Zhou, J.; Xing, W. Graphitized electrospun carbon fibers with superior cyclability as a free-standing anode of potassium-ion batteries. *J. Power Sources* **2020**, *474*, 228479. [CrossRef]

31. Wang, B.; Peng, Y.; Yuan, F.; Liu, Q.; Sun, L.; Zhang, P.; Wang, Q.; Li, Z.; Wu, Y.A. A comprehensive review of carbons anode for potassium-ion battery: Fast kinetic, structure stability and electrochemical. *J. Power Sources Sources* **2021**, *484*, 229244. [CrossRef]

32. Hirsh, H.S.; Li, Y.; Tan, D.H.; Zhang, M.; Zhao, E.; Meng, Y.S. Sodium-Ion Batteries Paving the way for grid energy storage. *Adv. Energy Mater.* **2020**, *10*, 2001274. [CrossRef]

33. Zhang, W.; Zhang, F.; Ming, F.; Alshareef, H.N. Sodium-ion battery anodes: Status and future trends. *Energy Chem* **2019**, *1*, 100012. [CrossRef]

34. Wang, L.; Światowska, J.; Dai, S.; Cao, M.; Zhong, Z.; Shen, Y.; Wang, M. Promises and challenges of alloy-type and conversion-type anode materials for sodium–ion batteries. *Mater. Today Energy* **2019**, *11*, 46–60. [CrossRef]

35. Qi, S.; Xu, B.; Tiong, V.T.; Hu, J.; Ma, J. Progress on iron oxides and chalcogenides as anodes for sodium-ion batteries. *Chem. Eng. J.* **2020**, *379*, 122261. [CrossRef]

36. Fiore, M.; Longoni, G.; Santangelo, S.; Pantò, F.; Stelitano, S.; Frontera, P.; Antonucci, P.L.; Ruffo, R. Electrochemical characterization of highly abundant, low cost iron(III) oxide as anode material for sodium-ion rechargeable batteries. *Electrochim. Acta* **2018**, *269*, 367–377. [CrossRef]

37. Modafferi, V.; Triolo, C.; Fiore, M.; Palella, A.; Spadaro, L.; Pianta, N.; Ruffo, R.; Patanè, S.; Santangelo, S.; Musolino, M.G. Effect of hematite doping with aliovalent impurities on the electrochemical performance of α-Fe$_2$O$_3$@rGO-based anodes in sodium–ion batteries. *Nanomaterials* **2020**, *10*, 1588. [CrossRef]

38. Wu, Z.G.; Zhong, Y.J.; Liu, J.; Wu, J.H.; Guo, X.D.; Zhong, B.H.; Zhang, Z.Y. Subunits controlled synthesis of α-Fe$_2$O$_3$ multi-shelled core–shell microspheres and their effects on lithium/sodium ion battery performances. *J. Mater. Chem. A* **2015**, *3*, 10092–10099. [CrossRef]

39. Santangelo, S.; Frontera, P.; Pantò, F.; Stelitano, S.; Marelli, M.; Malara, F.; Patané, S.; Dal Santo, V.; Antonucci, P.L. Effect of Ti- or Si-doping on nanostructure and photo-electro-chemical activity of electro-spun iron oxide fibres. *Int. J. Hydrogen Energy* **2017**, *42*, 28070–28081. [CrossRef]

40. Subramanian, A.; Gracia-Espino, E.; Annamalai, A.; Lee, H.H.; Lee, S.Y.; Choi, S.H.; Jang, J.S. Effect of tetravalent dopants on hematite nanostructure for enhanced photoelectrochemical water splitting. *Appl. Surf. Sci.* **2018**, *427*, 1203–1212. [CrossRef]

41. Zhao, L.; Xiao, J.; Huang, H.; Huang, Q.; Zhao, Y.; Li, Y. Enhanced efficiency of hematite photoanode for water splitting with the doping of Ge. *Int. J. Hydrogen Energy* **2018**, *43*, 12646–12652. [CrossRef]

42. Ponti, A.; Raza, M.H.; Pantò, F.; Ferretti, A.M.; Triolo, C.; Patanè, S.; Pinna, N.; Santangelo, S. Structure, defects and magnetism of electrospun hematite nanofibers silica-coated by atomic layer deposition. *Langmuir* **2020**, *36*, 1305–1319. [CrossRef] [PubMed]

43. Di Cicco, A.; Aquilanti, G.; Minicucci, M.; Principi, E.; Novello, N.; Cognigni, A.; Olivi, L. Novel XAFS capabilities at ELETTRA synchrotron light source. *J. Phys. Conf. Ser.* **2009**, *190*, 012043. [CrossRef]

44. Newville, M. IFEFFIT: Interactive XAFS analysis and FEFF fitting. *J. Synchrotron Rad.* **2001**, *8*, 322–324. [CrossRef] [PubMed]

45. Ravel, B.; Newville, M. ATHENA, ARTEMIS, HEPHAESTUS: Data analysis for X-ray absorption spectroscopy using IFEFFIT. *J. Synchrotron Rad.* **2005**, *12*, 537–541. [CrossRef]

46. Binitha, G.; Soumya, M.S.; Madhavan, A.A.; Praveen, P.; Balakrishnan, A.; Subramanian, K.R.V.; Reddy, M.V.; Shantikumar, V.N.; Sreekumaran, A.N.; Sivakumar, N. Electrospun α-Fe$_2$O$_3$ nanostructures for supercapacitor applications. *J. Mater. Chem. A* **2013**, *38*, 11698–11704. [CrossRef]

47. Chaudhari, S.; Srinivasan, M. 1D hollow α-Fe₂O₃ electrospun nanofibers as high performance anode material for lithium ion batteries. *J. Mater. Chem.* **2012**, *22*, 23049–23056. [CrossRef]

48. Li, N.; Jayaraman, S.; Tee, S.Y.; Kumar, P.S.; Lee, C.J.J.; Liew, S.L.; Chi, D.; Hor, T.S.A.; Ramakrishna, S.; Luo, H.K. Effect of La-Doping on optical bandgap and photoelectrochemical performance of hematite nanostructures. *J. Mater. Chem. A* **2014**, *45*, 19290–19297. [CrossRef]

49. Saveh-Shemshaki, N.; Latifi, M.; Bagherzadeh, R.; Malekshahi Byranvand, M.; Naseri, N.; Dabirian, A. Synthesis of mesoporous functional hematite nanofibrous photoanodes by electrospinning. *Polym. Adv. Technol.* **2016**, *27*, 358–365. [CrossRef]

50. Wu, R.A.; Lin, C.W.; Tseng, W.J. Preparation of electrospun Cu-doped α-Fe₂O₃ semiconductor nanofibers for NO₂ gas sensor. *Ceram. Int.* **2017**, *43*, S535–S540. [CrossRef]

51. Balbuena, J.; Cruz-Yusta, M.; Cuevas, A.L.; Martín, F.; Pastor, A.; Romero, R.; Sánchez, L. Hematite porous architectures as enhanced air purification photocatalyst. *J. Alloys Compd.* **2019**, *797*, 166–173. [CrossRef]

52. Wang, H.G.; Zhou, Y.; Shen, Y.; Li, Y.; Zuo, Q.; Duan, Q. Fabrication, formation mechanism and the application in lithium-ion battery of porous Fe₂O₃ nanotubes via single-spinneret electrospinning. *Electrochim. Acta* **2015**, *158*, 105–112. [CrossRef]

53. Ristic, M.; Kremenovic, A.; Reissner, M.; Petrovic, Z.; Music, S. Microstructural and magnetic properties of electrospun hematite/cuprospinel composites. *J. Mater. Sci. Mater. Electron.* **2020**, *31*, 9812–9825. [CrossRef]

54. Mou, F.; Guan, J.G.; Shi, W.; Sun, Z.; Wang, S. Oriented contraction: A facile nonequilibrium heat-treatment approach for fabrication of maghemite fiber-in-tube and tube-in-tube nanostructures. *Langmuir* **2010**, *26*, 15580–15585. [CrossRef]

55. Allieta, M.; Marelli, M.; Malara, F.; Bianchi, C.L.; Santangelo, S.; Triolo, C.; Patane, S.; Ferretti, A.M.; Kmente, Š.; Pontia, A.; et al. Shaped-controlled silicon-doped hematite nanostructures for enhanced PEC water splitting. *Catal. Today* **2019**, *328*, 43–49. [CrossRef]

56. Liu, J.; Cai, Y.Y.; Tian, Z.F.; Ruan, G.S.; Ye, Y.X.; Liang, C.H.; Shao, G.S. Highly oriented Ge-doped hematite nanosheet arrays for photoelectrochemical water oxidation. *Nano Energy* **2014**, *9*, 282–290. [CrossRef]

57. Zhu, Y.; Zhang, J.C.; Zhai, J.; Jiang, L. Preparation of superhydrophilic α-Fe₂O₃ nanofibers with tunable magnetic properties. *Thin Solid Films* **2006**, *510*, 271–274. [CrossRef]

58. Singh, B.P.; Kumar, A.; Areizaga-Martinez, H.I.; Vega-Olivencia, C.A.; Tomar, M.S. Synthesis, characterization, and electrocatalytic ability of γ-Fe₂O₃ nanoparticles for sensing acetaminophen. *Indian J. Pure Appl. Phys.* **2017**, *55*, 722–728.

59. Wang, J.; Zhou, H.; Zhuang, J.; Liu, Q. Magnetic γ-Fe₂O₃, Fe₃O₄, and Fe nanoparticles confined within ordered mesoporous carbons as efficient microwave absorbers. *Phys. Chem. Chem. Phys* **2015**, *17*, 3802–3812. [CrossRef] [PubMed]

60. Inamdar, S.N.; Haram, S.K. Synthesis and Characterization of Uncapped γ-Fe₂O₃ Nanoparticles Prepared by Flame Pyrolysis of Ferrocene in Ethanol. *J. Nanosci. Nanotechnol.* **2006**, *6*, 2155–2158. [CrossRef]

61. Chahal, S.; Kumar, A.; Kumar, P. Zn Doped α-Fe₂O₃: An efficient material for UV driven photocatalysis and electrical conductivity. *Crystals* **2020**, *10*, 273.

62. Bouhjar, F.; Mollar, M.; Chourou, M.L.; Marí, B.; Bessais, B. Hydrothermal synthesis of nanostructured Cr-doped hematite with enhanced photoelectrochemical activity. *Electrochim. Acta* **2018**, *260*, 838–846. [CrossRef]

63. Cao, Z.; Qin, M.; Gu, Y.; Jia, B.; Chen, P.; Qu, X. Synthesis and characterization of Sn-doped hematite as visible light photocatalyst. *Mater. Res. Bull.* **2016**, *77*, 41–47. [CrossRef]

64. Chernyshova, I.V.; Hochella, M.F., Jr.; Madden, A.S. Size-dependent structural transformations of hematite nanoparticles. 1. Phase transition. *Phys. Chem. Chem. Phys.* **2007**, *9*, 1736–1750. [CrossRef]

65. Jubb, A.M.; Allen, H.C. Vibrational spectroscopic characterization of hematite, maghemite, and magnetite thin films produced by vapor deposition. *ACS Appl. Mater. Interf.* **2010**, *2*, 2804–2812. [CrossRef]

66. Serrano, A.; Fernandez, J.F.; de la Fuente, O.R.; García, M.A. A novel route to obtain metal and oxide nanoparticles co-existing on a substrate. *Mater. Today Chem.* **2017**, *4*, 64–72. [CrossRef]

67. Massey, M.J.; Baier, U.; Merlin, R.; Weber, W.H. Effects of pressure and isotopic substitution on the Raman spectrum of α-Fe₂O₃: Identification of two-magnon scattering. *Phys. Rev. B* **1990**, *41*, 7822. [CrossRef]

68. Ahmmad, B.; Leonard, K.; Islam, M.S.; Kurawaki, J.; Muruganandham, M.; Ohkubo, T.; Kuroda, Y. Green synthesis of mesoporous hematite (α-Fe₂O₃) nanoparticles and their photocatalytic activity. *Adv. Powder Technol.* **2013**, *24*, 160–167. [CrossRef]

69. Marshall, C.P.; Dufresne, W.J.; Rufledt, C.J. Polarized Raman spectra of hematite and assignment of external modes. *J. Raman Spectrosc.* **2020**, *51*, 1522–1529. [CrossRef]

70. Zoppi, A.; Lofrumento, C.; Castellucci, E.M.; Sciau, P. Al-for-Fe substitution in hematite: The effect of low Al concentrations in the Raman spectrum of Fe₂O₃. *J. Raman Spectrosc.* **2008**, *39*, 40–46. [CrossRef]

71. Bersani, D.; Lottici, P.P.; Montenero, A. Micro-Raman investigation of iron oxide films and powders produced by sol–gel syntheses. *J. Raman Spectrosc.* **1999**, *30*, 355–360. [CrossRef]

72. Testa-Anta, M.; Ramos-Docampo, M.A.; Comesaña-Hermo, M.; Rivas-Murias, B.; Salgueiriño, V. Raman spectroscopy to unravel the magnetic properties of iron oxide nanocrystals for bio-related applications. *Nanoscale Adv.* **2019**, *1*, 2086–2103. [CrossRef]

73. Chaudhari, N.S.; Warule, S.S.; Muduli, S.; Kale, B.B.; Jouen, S.; Lefez, B.; Hannoyer, B.; Ogale, S.B. Maghemite (hematite) core (shell) nanorods via thermolysis of a molecular solid of Fe-complex. *Dalton Trans.* **2011**, *40*, 8003–8011. [CrossRef]

74. El Mendili, Y.; Grasset, F.; Randrianantoandro, N.; Nerambourg, N.; Greneche, J.M.; Bardeau, J.F. Improvement of thermal stability of maghemite nanoparticles coated with oleic acid and oleylamine molecules: Investigations under laser irradiation. *J. Phys. Chem. C* **2015**, *119*, 10662–10668. [CrossRef]

75. Yan, W.; Fan, H.; Zhai, Y.; Yang, C.; Ren, P.; Huang, L. Low temperature solution-based synthesis of porous flower-like-Fe_2O_3 superstructures and their excellent gas-sensing properties. *Sens. Actuators B* **2011**, *160*, 1372–1379. [CrossRef]

76. Huang, Z.; Cheng, J.; Ren, X.; Zhuang, J.; Roy, V.A.; Burkhartsmeyer, J.M.; Wong, K.S.; Choy, W.C. All-room-temperature solution-processed new nanocomposites based hole transport layer from synthesis to film formation for high-performance organic solar cells towards ultimate energy-efficient fabrication. *Nano Energy* **2018**, *47*, 26–34. [CrossRef]

77. Zhang, J.; Yu, T.; Chen, J.; Liu, H.; Su, D.; Tang, Z.; Xie, J.; Chen, L.; Yuan, A.; Kong, Q. Germanium-based complex derived porous GeO_2 nanoparticles for building high performance Li-ion batteries. *Ceram. Int.* **2018**, *44*, 1127–1133. [CrossRef]

78. Phani, A.R.; Di Claudio, D.; Passacantando, M.; Santucci, S. GeO_2 based high k dielectric material synthesized by sol–gel process. *J. Non-Cryst Solids* **2007**, *353*, 692–696. [CrossRef]

79. Mura, A.; Hideshima, I.; Liu, Z.; Hosoi, T.; Watanabe, H.; Arima, K. Water growth on GeO_2/Ge (100) stack and its effect on the electronic properties of GeO_2. *J. Phys. Chem. C* **2013**, *117*, 165–171. [CrossRef]

80. Jain, S.; Shah, J.; Negi, N.S.; Sharma, C.; Kotnala, R.K. Significance of interface barrier at electrode of hematite hydroelectric cell for generating ecopower by water splitting. *Int. J. Energy Res.* **2019**, *43*, 4743–4755. [CrossRef]

81. Spadaro, L.; Palella, A.; Arena, F. Copper-Iron-Zinc-Cerium oxide compositions as most suitable catalytic materials for the synthesis of green fuels via CO_2 hydrogenation. *Catal. Today* **2020**. [CrossRef]

82. Palella, A.; Spadaro, L.; Di Chio, R.; Arena, F. Effective low-temperature catalytic methane oxidation over $MnCeO_x$ catalytic compositions. *Catal. Today* **2020**. [CrossRef]

83. Patra, D.; Gopalan, B.; Ganesan, R. Direct solid-state synthesis of maghemite as a magnetically recoverable adsorbent for the abatement of methylene blue. *J. Environ. Chem. Eng.* **2019**, *7*, 103384. [CrossRef]

84. Magro, M.; Molinari, S.; Venerando, A.; Baratella, D.; Zoppellaro, G.; Salviulo, G.; Zboril, R.; Vianello, F. Colloidal maghemite nanoparticles with oxyhydroxide-like interface and chiroptical properties. *Appl. Surf. Sci.* **2020**, *534*, 147567. [CrossRef]

85. Coduri, M.; Masala, P.; Del Bianco, L.; Spizzo, F.; Ceresoli, D.; Castellano, C.; Cappelli, S.; Oliva, C.; Checchia, S.; Allieta, M.; et al. Local Structure and Magnetism of Fe_2O_3 Maghemite Nanocrystals: The Role of Crystal Dimension. *Nanomaterials* **2020**, *10*, 867. [CrossRef]

86. Fracchia, M.; Visibile, A.; Ahlberg, A.; Vertova, A.; Minguzzi, A.; Ghigna, P.; Rondinini, S. α- and γ-FeOOH: Stability, Reversibility, and Nature of the Active Phase under Hydrogen Evolution. *ACS Appl. Energy Mater.* **2018**, *1*, 1716–1725. [CrossRef]

87. Wilke, M.; Farges, F.; Petit, P.E.; Brown, G.E., Jr.; Martin, F. Oxidation state and coordination of Fe in minerals: An Fe K-XANES spectroscopic study. *Am. Mineral.* **2001**, *86*, 714–730. [CrossRef]

88. Bertini, L.; Ghigna, P.; Scavini, M.; Cargnonia, F. Germanium K edge in GeO_2 polymorphs. Correlation between local coordination and electronic structure of germanium. *Phys. Chem. Chem. Phys.* **2003**, *5*, 1451–1456. [CrossRef]

89. Mastelaro, V.R.; Zanotto, E.D. X-ray Absorption Fine Structure (XAFS) Studies of Oxide Glasses—A 45-Year Overview. *Materials* **2018**, *11*, 204. [CrossRef]

90. Hill, A.H.; Jiao, F.; Bruce, P.G.; Harrison, A.; Kockelmann, W.; Ritter, C. Neutron diffraction study of mesoporous and bulk hematite, α-Fe_2O_3. *Chem. Mater.* **2008**, *20*, 4891–4899. [CrossRef]

91. Ritter, C. Neutrons not entitled to retire at the age of 60: More than ever needed to reveal magnetic structures. *Solid State Phenom.* **2011**, *170*, 263–269. [CrossRef]

92. Graves, J. A powder neutron diffraction investigation of vacancy ordering and covalence in γ-Fe_2O_3. *Sol. St. Chem.* **1983**, *49*, 325–333. [CrossRef]

93. Yu, L.; Hu, R.; Sang, X.; Liu, J.; Thomas, M.P.; Hudak, B.M.; Patel, A.; Page, K.; Guilton, B.S. Shell-induced Ostwald ripening: Simultaneous structure, composition, and morphology transformations during the creation of hollow iron oxide nanocapsules. *ACS Nano* **2018**, *12*, 9051–9059. [CrossRef]